Analysis of the electronic and chemical structure in boron and phosphorus passivated *4H*-SiC/SiO_2 interfaces using HRTEM and STEM-EELS

Joshua A. Taillon,[1,a)] Christopher J. Klingshirn,[1] Chunkun Jiao,[2] Yongju Zheng,[2] Sarit Dhar,[2] Tsvetanka S. Zheleva,[3] Aivars J. Lelis,[3] and Lourdes G. Salamanca-Riba[1,b)]
[1]*Department of Materials Science and Engineering, University of Maryland, College Park, Maryland 20742, USA*
[2]*Department of Physics, Auburn University, Auburn, Alabama 36849, USA*
[3]*US Army Research Laboratory, Adelphi, Maryland 20783, USA*

(Received 23 August 2018; accepted 23 October 2018; published online 7 November 2018)

We report a transmission electron microscopy (TEM) study of the impacts of phosphorus and boron passivation processes at *4H*-SiC/SiO_2 interfaces. The chemical and electronic structures at these interfaces have been analyzed using high-resolution TEM and spatially resolved electron energy-loss spectroscopy (EELS), uncovering a range of phenomena caused by the presence of B and P within their respective boro- and phosphosilicate glass (BSG/PSG) layers. The phosphorus passivation process was observed to induce roughness at the SiC/PSG interface on the order of 100s of nm. Within the PSG layer, phosphorus was found to segregate into nanometer-scale P-rich clusters, contradicting previous reports that it is distributed uniformly throughout the PSG. Similar to N in nitric oxide annealed devices, boron was determined to accumulate in a thin layer (sub-3 nm in thickness) at the SiC/BSG interface, with a much narrower distribution than previously reported. EELS measurements indicated boron incorporates in a trigonal bonding configuration, supporting the assertion that it softens the oxide and causes significant stress reduction at the interface with *4H*-SiC. These results supply further insight into the sources of mobility enhancement in PSG and BSG-gated devices that could be extended into additional improvement in the channel response of SiC MOSFETs. *Published by AIP Publishing.* https://doi.org/10.1063/1.5053595

Due to its wide bandgap (3.23 eV), native SiO_2 oxide, high bulk electron mobility, and high thermal conductivity, *4H*-SiC is a prevalent material for high power/temperature metal oxide semiconductor (MOS) devices.[1,2] In traditional thermally oxidized SiC MOS devices, the inversion layer field-effect mobility (μ_{FE}) is reduced by a high density of trap states (D_{it}) caused by electrically active defects at the *4H*-SiC/SiO_2 interface, diminishing MOSFET performance.[3–8] The successful commercialization of *4H*-SiC MOSFETs can be attributed to the discovery of the high-temperature nitric oxide (NO) post-oxidation anneal (POA) process.[4,9,10] Nitridation of the *4H*-SiC/SiO_2 interface lowers D_{it} and improves peak μ_{FE} from 5 cm^2/V s to 35 cm^2/V s by passivating the performance-limiting defects that induce states near the conduction band-edge of *4H*-SiC.[11] Nitridated interfaces have been well characterized, revealing that the N atoms preferentially accumulate in the interfacial region,[12–17] significantly modifying the bonding states of both Si and C at the interface, as well as the oxide states when using a-face SiC substrates.[18]

In recent years, a number of alternative processing strategies have been proposed to extend device performance beyond that enabled by the NO POA.[2] Two particularly promising methods of channel engineering are phosphorus and boron passivations. High-temperature annealing of the thermally grown SiO_2 in a P-containing ambient converts the SiO_2 layer to a phosphosilicate glass (PSG). This process improves μ_{FE} to approximately 75–105 cm^2/V s by a combination of low D_{it} and phosphorus channel surface doping, but the polar nature of the material induces voltage instabilities that ultimately limit the device's performance.[19–24]

The incorporation of boron into the SiC/SiO_2 interface has been shown to further enhance μ_{FE} values to approximately 100 cm^2/V s, which has been attributed to a reduction in interfacial stress at the SiC/borosilicate glass (BSG) interface.[25] Unlike with P, voltage instability issues are not observed in the B-treated devices,[26] but a performance-reliability tradeoff may exist between improved μ_{FE} and the positive threshold voltage (V_{th}) shift and bias-temperature instability effects that have been measured in both P- and B-doped devices.[22,27] Follow-up research has shown that in combination with an antimony-doped surface layer, boron treatment can result in μ_{FE} values up to 180 cm^2/V s,[27] while incorporation of boron together with nitridation and a deposited oxide layer enables peak μ_{FE} values up to 170 cm^2/V s.[28,29]

For both PSG and BSG treatments, the majority of characterization work has been electrical in nature, and very few physical or chemical investigations have been reported, in contrast to NO POA. In the case of phosphorus, secondary ion mass spectrometry (SIMS) has suggested the full conversion of SiO_2 into PSG, with a uniform concentration of P through the layer.[20,30] X-ray photoelectron spectroscopy (XPS) measurements have indicated a uniform atomic fraction for P of 5% within the PSG layer.[22] Using transmission electron microscopy (TEM), Fiorenza *et al.*[31] reported a similar finding of P "almost homogeneously distributed within

a)Present address: Material Measurement Laboratory, National Institute of Standards and Technology (NIST), Gaithersburg, MD 20899, USA. Electronic mail: joshua.taillon@nist.gov.
b)Electronic mail: riba@umd.edu.

the insulating layer" as measured with energy dispersive X-ray spectroscopy (TEM-EDS).

In the case of BSG passivation, existing compositional information in the literature has been acquired by SIMS, the results of which vary depending on each specific report. Okamoto *et al.*[25] reported a uniform B concentration ($3 \times 10^{20}\,cm^{-3}$) in the bulk of the BSG, and a 5 nm–10 nm wide "pileup" of boron at the interface with a peak concentration approximately 2.3 times that of the bulk BSG. Measuring samples identical to those used in the present work, Zheng *et al.*[27] reported a higher uniform concentration but without any pileup at the interface. Uniform concentrations both without[28] and with[29] interfacial concentration peaks have been reported for samples receiving nominally identical boron passivation and nitridation treatments, highlighting the well-known difficulty of interpreting SIMS data at interfaces.[32] Cross-sectional microscopy is a more direct and reliable means to inspect composition and structure at material boundaries, which is essential to better understand the origins of BSG-induced μ_{FE} enhancement as well as any associated drawbacks, such as an increase in V_{th} caused by B penetration into the SiC.[27]

In this work, 4° off-axis *4H*-SiC wafers with 10 μm thick *n*- (PSG) or *p*- (BSG) type homoepitaxial layers doped at $\sim 1 \times 10^{16}\,cm^{-3}$ were diced into 5 mm × 5 mm pieces. After standard RCA cleaning, the samples were thermally oxidized at 1150 °C to grow ~60 nm thick oxides. To create the PSG layers, the oxidized pieces were annealed at 1000 °C for 15 min in a gas mixture of $POCl_3$, O_2, and N_2 (flow ratio 3:4:9). These samples were further annealed in pure N_2 for 30 min to homogenize the PSG layer. To form BSG films, separate oxidized samples were annealed with a B_2O_3 planar diffusion source (Techneglas, GS-139) in a gas mixture of Ar (50 sccm) and O_2 (5 sccm) at 950 °C for 30 min, followed by a 2 h drive-in anneal at the same temperature in Ar without the B_2O_3. Metal contact pads were thermally evaporated onto the PSG/BSG surfaces for electrical measurements. Further processing specifics and detailed analyses of the samples' electrical qualities are available in Refs. 22 and 27 for the PSG and BSG samples, respectively.

High-resolution (HR) TEM was performed on cross-sectional TEM samples, along with Z-contrast high angle annular dark-field scanning TEM (HAADF-STEM) and electron energy-loss spectroscopy (EELS) using a JEOL JEM 2100F TEM/STEM equipped with a Gatan Tridiem imaging filter (GIF). Specimens were prepared using standard FIB procedures[33,34] with a Tescan Gaia FIB/SEM. TEM lamellae were polished to a final thickness between 20 nm and 50 nm using a 2 keV Ga^+ FIB.

EELS data were collected as areal spectrum images (SIs) at 200 keV in the STEM mode with 12.0 mrad convergence and 29.0 mrad collection semi-angles, with a probe size of 0.5 nm–0.7 nm. Multiple SIs were taken from different areas along each interface to validate interpretation of the data. Hyperspectral unmixing via non-negative matrix factorization (NMF) was used to analyze the EELS data.[35–40] NMF is an unsupervised machine learning technique able to separate EELS signals into physically interpretable components even when spectral features overlap.[37] The number of components to include was determined by inspection of the scree plot, and the analyses were performed using the *HyperSpy* software package.[41] This unmixing analysis separates the data into descriptive "component" spectra, together with "loading" maps which represent the relative intensity of each component in the spectrum image. The result is an additive model, where each pixel of the spectrum image is a weighted sum of the component spectra.

The interface in each sample was first imaged via HRTEM and HAADF-STEM (Fig. 1). Lower magnification TEM (not shown) revealed that the SiC/PSG interface roughness is much greater than at the SiC/SiO_2 interface without phosphorus, which is nearly flat aside from the miscut-angle.[16,18] PSG samples from varying SiC wafer stocks showed peak-to-valley amplitude oscillations of approximately 6 nm–7 nm with periods on the order of 100 s of nm, which may arise from uneven additional oxidation occurring during the $POCl_3$ anneal. Consequently, HRTEM [Fig. 1(a)] reveals significant atomic-scale roughness at the interface, and the PSG appears uniformly amorphous throughout the layer. The top surface of the PSG layer, however, is extremely flat, indicating that while the PSG anneal induces roughness at the SiC/PSG interface, the resultant PSG layer is softened enough to reflow during the anneal[31,42] and produce a smooth topography at the PSG surface.

In complementary HAADF-STEM imaging of the interfacial region and PSG layer shown in Fig. 1(b), contrast corresponds primarily to atomic mass, with brighter areas indicating higher mass due to greater scattering of incident electrons. Thus, the non-uniform darker region 5 nm–10 nm in thickness adjacent to the interface suggests a lower atomic mass in this area. The remainder of the PSG contains bright clusters a few nm in size, which are evidence of a heterogeneous mass distribution.

In order to better understand these morphological features, STEM-EELS data were collected from the interfacial and bulk PSG regions, providing insight into composition and electronic structure. Overlap between the fine structure of the Si-$L_{2,3}$ and P-$L_{2,3}$ edges prevents traditional EELS analysis methods (background subtraction and edge integration) from isolating the P contributions, requiring the use of spectral unmixing methods. An NMF analysis of the Si-$L_{2,3}$ and P-$L_{2,3}$ edges without prior background subtraction is shown in Fig. 2. Five components were unmixed and each (together with its loading map) can be ascribed to a particular source within the EELS data. The first component (blue)

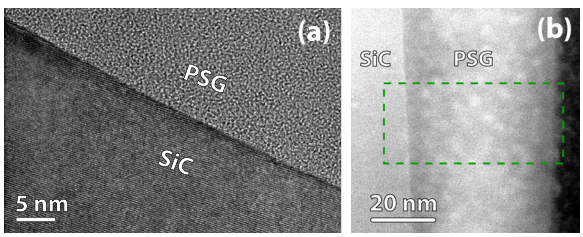

FIG. 1. HRTEM and HAADF-STEM from a P-passivated SiC MOS device. (a) HRTEM image of the SiC/PSG interface, showing many atomic steps due to the long-range roughness. (b) HAADF-STEM (Z-contrast) image of the SiC/PSG interface, with the contrast enhanced to illustrate the presence of bright spots distributed throughout the PSG, and the dark layer (lower mass) at the interface. The green box indicates the area from which the EELS data in Fig. 2 were collected.

captures most of the inelastic scattering background arising from the Si in both the SiC and PSG. The second (green) is dominant within the substrate and matches the expectations for Si in SiC. The remaining three signals all have a Si-$L_{2,3}$ edge resembling SiO_2, but with variations in the fine structure.

Among these oxide-like signals, the first (red) is localized to the brighter clusters in the STEM image. Given the greater atomic mass of P compared to Si and O, it is expected that these bright clusters indicate P-rich regions of the PSG layer. Indeed, a subtle but definite edge is observed in the spectrum of this component near 132 eV, corresponding to the onset energy of the P-$L_{2,3}$ edge. P-rich clusters appear randomly distributed throughout the PSG layer, with an average diameter of 3.6 ± 0.8 nm. There is also a distinct decrease in the intensity of the phosphorus component within approximately 5 nm of the interface, correlating well with the dark layer observed in Fig. 1(b) and suggesting a more SiO_2-like character close to the interface. This result conflicts with prior SIMS and EDS studies reporting a uniform P concentration throughout the PSG,[20,31] but the EELS mapping method used in the present work is expected to have much higher lateral resolution and sensitivity than the previous methods, which average over a wide area.

The energy-loss near-edge structure (ELNES) of the phosphorus component reveals information about the bonding environment and arrangement of P atoms within the PSG layer.[43] As marked by the red arrow in Fig. 2, the edge onset energy of the phosphorus component is ~2 eV below the energy of 132 eV expected from a pure phosphorus oxide such as P_2O_5.[44] The reduced edge onset indicates a reduction in the oxidation state of phosphorus, potentially arising from P substituting at an O site in SiO_2.[45] Additionally, a Si-$L_{2,3}$ edge consistent with that of SiO_2 is still visible in the P-containing component. This EELS evidence implies that P is present together with SiO_2, but since the EELS signal is averaged throughout the projected thickness of the lamella, a complete separation of the phases cannot be ruled out.

The remaining two NMF components (purple and yellow in Fig. 2) are spectrally similar, akin to the EEL spectrum of SiO_2. The first has an onset energy 2 eV higher than the second. The peak with an onset at 105.7 eV (clearly present in *Oxide 1*, but less so in *Oxide 2*) results from the excitonic transition in tetrahedral SiO_4 bonding units.[46] The shift of intensity to lower energy in *Oxide 2* suggests reduced oxygen coordination, typical in SiO_x sub-stoichiometric oxides.[46,47]

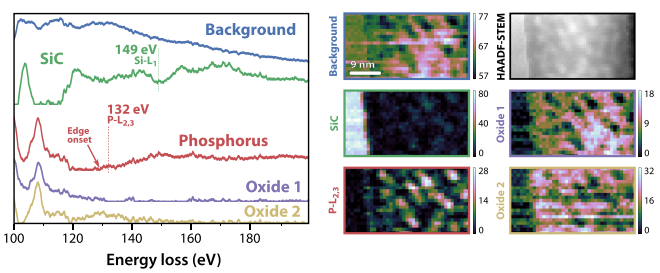

FIG. 2. Hyperspectral unmixing analysis of the SiC/PSG interface at the Si-$L_{2,3}$ (99 eV) and P-$L_{2,3}$ (132 eV) edges. NMF decomposition resulted in five components (left). Loading maps (right) reveal spectral intensity at the P-$L_{2,3}$ edge in the bright clusters of the HAADF-STEM image (Fig. 1 and top right), indicating that they are P-rich.

The loading maps of these two components indicate that *Oxide 2* has greater intensity closer to the SiC/PSG interface, while *Oxide 1* is most intense approximately 15 nm from the interface.

The non-homogeneous distribution of phosphorus throughout the PSG layer is unexpected and contrasts with prior TEM studies.[31] The impacts of such a distribution on the electrical properties of PSG-passivated MOS devices are not immediately clear although it is possible that such non-uniformity could give rise to the observed performance-limiting polarization instabilities.[20] The presence of these clusters raises the possibility of tuning their shape and distribution, which should be further investigated as a means to engineer the oxide and channel response of PSG-passivated SiC MOSFETs.

Contrary to the phosphorus-annealed samples, the BSG films were significantly more uniform, as shown in Fig. 3. Figure 3(a) reveals a nearly flat interface of similar quality to that observed in NO-annealed devices.[16,18] Notably, the BSG interface does not show the large-scale undulations observed at the SiC/PSG interface.

STEM-EELS measurements were used to further probe the chemical makeup of the BSG interfacial region. The spectrum image displayed in Fig. 4 profiles the B-*K* edge through approximately 15 nm of the BSG layer in a second BSG sample prepared under similar conditions.

Following subtraction of the power-law background before the Si-$L_{2,3}$ edge, two NMF components were required to capture the spectral features near the B-*K* edge. The first component (blue in Fig. 4) is strongest within the SiC substrate and is attributed to residual inelastic scattering background and signal from the extended structure of the Si-L_1 edge. The second component (green) matches the expected shape of the B-*K* edge,[48] confirming the presence of boron within the BSG layer. The loading map for this component shows boron concentrated at the interface. Each component was summed parallel to the interface and plotted as a linear profile of relative intensity in Fig. 4(b) to illustrate this phenomenon. As expected, the SiC component intensity drops sharply across the interface. The boron profile exhibits a distinct peak approximately 1 nm from the SiC/BSG interface, with an intensity about twice that within the bulk BSG.

The ELNES of the measured B-*K* signal provides insight into the configuration of the boron atoms at the interface and within the BSG layer. In seven spectrum images analyzed, the primary boron component peak is measured at 193.8 ± 0.7 eV, in close agreement with the previously reported energy of

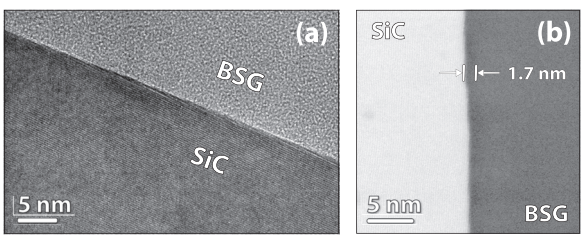

FIG. 3. (a) HRTEM image of the SiC/BSG interface, showing atomic steps arising from the 4° substrate miscut angle. (b) High-magnification HAADF-STEM (Z-contrast) image of the SiC/BSG interface, with contrast enhanced to illustrate the presence of an ~1.7 nm wide dark layer at the interface.

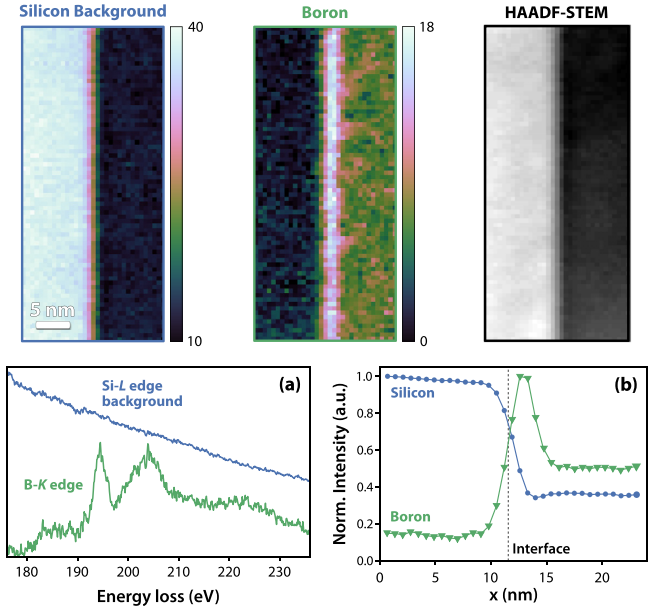

FIG. 4. Hyperspectral unmixing analysis of the SiC/BSG interface. (a) The two NMF-identified components, attributed to SiC and boron. Loading maps of each component are displayed at the top of the figure, together with the simultaneously collected HAADF-STEM signal which shows an ∼2.1 nm wide dark layer at the interface. (b) Normalized line profiles summed parallel to the interface for each component. The B-*K* signal peaks adjacent to the SiC/BSG interface (FWHM = 2.8 nm), with a boron concentration approximately twice that of the bulk BSG.

the π^* antibonding orbital, indicative of sp^2 hybridized boron.[48] The energy of this peak matches those of B_2O_3[48] and BO_3.[49] No difference was found in the B-*K* signal near the interface compared to within the BSG bulk, implying that the boron atoms' bonding states are similar between them. Repeated unmixing analyses with additional components also failed to detect any difference between the interfacial and BSG boron, yielding only higher-order noise components.

With sub-nanometer resolution, the present EELS results show a boron peak with a full width at half maximum (FWHM) of 2.8 ± 0.7 nm, slightly wider than the dark layers observed using HAADF-STEM imaging [Figs. 3(b) and 4]. This finding contrasts with previously reported SIMS data which suggested either a significantly wider (∼7 nm) peak in B concentration[25,29] or no peak at all,[27,28] but the present results are expected to be more reliable than the previously reported SIMS results, as discussed earlier.

The distribution of boron throughout the BSG layer is expected to have significant impacts on device performance. The trigonal bonding configuration revealed by the B-*K* ELNES confirms boron's role as a network former within the oxide layer, resulting in a higher concentration of non-bonding oxygen atoms.[50] These network modifications result in weaker bonds within the glassy layer that are softer and more fluid than pure SiO_2. Since the boron concentration peaks at the interface, the thin interfacial layer is likely more capable of relieving interfacial stresses than SiO_2 (and the bulk BSG), supporting the interfacial stress relief mechanism for reduced D_{it} proposed in Ref. 25. Definitive evidence of stress relief, however, would require further studies at higher resolution, such as by aberration-corrected TEM.

We have reported HRTEM and STEM-EELS characterizations of *4H*-SiC devices treated with potential next-generation phosphorus and boron passivations. EELS data were processed using a spectral unmixing strategy, enabling detailed analysis of significantly overlapping ELNES features. Contrary to devices processed using standard NO annealing, bulk oxide effects were found to be dominant in the PSG samples. HRTEM measurements revealed much larger roughness at the interface due to near μm-scale undulations induced by the PSG passivation process. Phosphorus was observed to be distributed heterogeneously throughout the oxide layer, and the chemical signature of the SiO_2 signal varied as a function of distance from the SiC/PSG interface. Conversely in the BSG sample, boron was determined to accumulate in a few-nm layer at the interface, with a narrower distribution than previously measured by SIMS. The ELNES features at the B-*K* edge revealed boron to be trigonally coordinated, supporting the stress-relief mechanism of BSG mobility enhancement proposed in the prior literature. Further work analyzing the stress and strain at these interfaces is needed to definitely confirm this argument.

The authors gratefully acknowledge the support of the Maryland NanoCenter/AIMLab and funding by the U.S. Army Research Laboratory (No. W911NF-14-2-0110). J.A.T. acknowledges support through the NSF GRFP (No. DGE1322106). S.D. acknowledges the support of the II-VI Foundation Block Gift Program. Commercial products identified in this text are not recommendations or endorsement by NIST, nor are they necessarily the best available for the stated purpose.

[1]M. Bhatnagar and B. Baliga, IEEE Trans. Electron Devices **40**, 645 (1993).
[2]G. Liu, B. R. Tuttle, and S. Dhar, Appl. Phys. Rev. **2**, 021307 (2015).
[3]R. Schörner, P. Friedrichs, D. Peters, and D. Stephani, IEEE Electron Device Lett. **20**, 241 (1999).
[4]G. Y. Chung, C. C. Tin, J. R. Williams, K. McDonald, M. Di Ventra, S. T. Pantelides, L. C. Feldman, and R. A. Weller, Appl. Phys. Lett. **76**, 1713 (2000).
[5]K. C. Chang, J. Bentley, and L. M. Porter, J. Electron. Mater. **32**, 464 (2003).
[6]X. Shen, M. P. Oxley, Y. Puzyrev, B. R. Tuttle, G. Duscher, and S. T. Pantelides, J. Appl. Phys. **108**, 123705 (2010).
[7]M. Di Ventra and S. T. Pantelides, J. Electron. Mater. **29**, 353 (2000).
[8]C. J. Cochrane, P. M. Lenahan, and A. J. Lelis, Appl. Phys. Lett. **100**, 023509 (2012).
[9]H.-F. Li, S. Dimitrijev, H. Harrison, and D. Sweatman, Appl. Phys. Lett. **70**, 2028 (1997).
[10]J. Rozen, in *Physics and Technology of Silicon Carbide Devices*, edited by Y. Hijikata (InTech, 2012), Chap. 10, pp. 251–278.
[11]G. Y. Chung, C. C. Tin, J. R. Williams, K. McDonald, R. K. Chanana, R. A. Weller, S. T. Pantelides, L. C. Feldman, O. W. Holland, M. K. Das, and J. W. Palmour, IEEE Electron Device Lett. **22**, 176 (2001).
[12]H.-F. Li, S. Dimitrijev, D. Sweatman, H. B. Harrison, P. Tanner, and B. Feil, J. Appl. Phys. **86**, 4316 (1999).
[13]S. Dhar, Y. W. Song, L. C. Feldman, T. Isaacs-Smith, C. C. Tin, J. R. Williams, G. Y. Chung, T. Nishimura, D. Starodub, T. Gustafsson, and E. C. Garfunkel, Appl. Phys. Lett. **84**, 1498 (2004).
[14]K. McDonald, R. A. Weller, S. T. Pantelides, L. C. Feldman, G. Y. Chung, C. C. Tin, and J. R. Williams, J. Appl. Phys. **93**, 2719 (2003).
[15]K. C. Chang, Y. Cao, L. M. Porter, J. Bentley, S. Dhar, L. C. Feldman, and J. R. Williams, J. Appl. Phys. **97**, 104920 (2005).
[16]J. A. Taillon, J. H. Yang, C. A. Ahyi, J. Rozen, J. R. Williams, L. C. Feldman, T. S. Zheleva, A. J. Lelis, and L. G. Salamanca-Riba, J. Appl. Phys. **113**, 044517 (2013).

[17]J. Houston Dycus, W. Xu, D. J. Lichtenwalner, B. Hull, J. W. Palmour, and J. M. Lebeau, Appl. Phys. Lett. **108**, 201607 (2016).
[18]J. A. Taillon, "Applications of advanced analytical microscopy at the nanoscale: Wide bandgap and solid oxide fuel cell materials," Ph.D. thesis (University of Maryland, 2016).
[19]D. Okamoto, H. Yano, K. Hirata, T. Hatayama, and T. Fuyuki, IEEE Electron Device Lett. **31**, 710 (2010).
[20]Y. K. Sharma, C. A. Ahyi, T. Isaacs-Smith, X. Shen, S. T. Pantelides, X. Zhu, L. C. Feldman, J. Rozen, and J. R. Williams, Solid-State Electron. **68**, 103 (2012).
[21]Y. K. Sharma, A. C. Ahyi, T. Isaacs-Smith, A. Modic, M. Park, Y. Xu, E. L. Garfunkel, S. Dhar, L. C. Feldman, and J. R. Williams, IEEE Electron Device Lett. **34**, 175 (2013).
[22]C. Jiao, A. C. Ahyi, C. Xu, D. Morisette, L. C. Feldman, and S. Dhar, J. Appl. Phys. **119**, 155705 (2016).
[23]D. Okamoto, H. Yano, T. Hatayama, and T. Fuyuki, Appl. Phys. Lett. **96**, 203508 (2010).
[24]A. Jayawardena, X. Shen, P. M. Mooney, and S. Dhar, Semicond. Sci. Technol. **33**, 065005 (2018).
[25]D. Okamoto, M. Sometani, S. Harada, R. Kosugi, Y. Yonezawa, and H. Yano, IEEE Electron Device Lett. **35**, 1176 (2014).
[26]D. Okamoto, M. Sometani, S. Harada, R. Kosugi, Y. Yonezawa, and H. Yano, Appl. Phys. A **123**, 133 (2017).
[27]Y. Zheng, T. Isaacs-Smith, A. C. Ahyi, and S. Dhar, IEEE Electron Device Lett. **38**, 1433 (2017).
[28]M. Cabello, V. Soler, N. Mestres, J. Montserrat, J. Rebollo, J. Millán, and P. Godignon, Mater. Sci. Forum **897**, 352 (2017).
[29]M. Cabello, V. Soler, J. Montserrat, J. Rebollo, J. M. Rafí, and P. Godignon, Appl. Phys. Lett. **111**, 042104 (2017).
[30]Y. Jia, H. Lv, X. Tang, Q. Song, Y. Zhang, Y. Zhang, S. Dimitrijev, and J. Han, "Growth and characterization of nitrogen-phosphorus hybrid passivated gate oxide film of N-type 4H-SiC epilayer," J. Crystal Growth (in press).
[31]P. Fiorenza, L. K. Swanson, M. Vivona, F. Giannazzo, C. Bongiorno, A. Frazzetto, and F. Roccaforte, Appl. Phys. A: Mater. Sci. Process. **115**, 333 (2014).
[32]F. Stevie, *Secondary Ion Mass Spectrometry: Applications for Depth Profiling and Surface Characterization* (Momentum Press, 2015) p. 262.
[33]M. Schaffer, B. Schaffer, and Q. Ramasse, Ultramicroscopy **114**, 62 (2012).
[34]J. A. Taillon, V. Ray, and L. G. Salamanca-Riba, Microsc. Microanal. **23**, 872 (2017).
[35]D. D. Lee and H. S. Seung, Nature **401**, 788 (1999).
[36]N. Bonnet, N. Brun, and C. Colliex, Ultramicroscopy **77**, 97 (1999).
[37]N. Bonnet and D. Nuzillard, Ultramicroscopy **102**, 327 (2005).
[38]N. Dobigeon and N. Brun, Ultramicroscopy **120**, 25 (2012).
[39]O. Nicoletti, F. de la Peña, R. K. Leary, D. J. Holland, C. Ducati, and P. A. Midgley, Nature **502**, 80 (2013).
[40]P. M. Voyles, Curr. Opin. Solid State Mater. Sci. **21**, 141 (2017).
[41]F. de la Peña, T. Ostasevicius, V. T. Fauske, P. Burdet, P. Jokubauskas, M. Nord, M. Sarahan, D. N. Johnstone, E. Prestat, J. A. Taillon *et al.*, "hyperspy/hyperspy v1.2," (2017).
[42]O. K. T. Wu and A. N. Saxena, J. Electrochem. Soc. **132**, 932 (1985).
[43]V. J. Keast, A. J. Scott, R. Brydson, D. Williams, and J. Bruley, J. Microsc. **203**, 135 (2001).
[44]J. Gao, Q. Zhao, Y. Sun, G. Li, J. Zhang, and D. Yu, Nanoscale Res. Lett. **6**, 45 (2010).
[45]V. Vaithianathan, K. Asokan, J. Y. Park, and S. S. Kim, Appl. Phys. A **94**, 995 (2009).
[46]P. E. Batson, Microsc., Microanal., Microstruct. **2**, 395 (1991).
[47]D. A. Muller, Ultramicroscopy **78**, 163 (1999).
[48]R. Arenal, F. de la Peña, O. Stéphan, M. Walls, M. Tencé, A. Loiseau, and C. Colliex, Ultramicroscopy **109**, 32 (2008).
[49]P. A. Bingham, G. Yang, R. J. Hand, and G. Mobus, Solid State Sci. **10**, 1194 (2008).
[50]R. A. Smith, J. Non-Cryst. Solids **84**, 421 (1986).